# Core structure and Peierls stress of edge and screw dislocations in TiN: A density functional theory study

S.K. Yadav [a,b], R. Ramprasad [b], A. Misra [c], X.-Y. Liu [a,*]

[a] *Materials Science and Technology Division, MST-8, Los Alamos National Laboratory, Los Alamos, NM 87545, USA*
[b] *Materials Science and Engineering, University of Connecticut, Storrs, CT 06269, USA*
[c] *Materials Physics and Applications Division, MPA-CINT, Los Alamos National Laboratory, Los Alamos, NM 87545, USA*

## Abstract

A first-principles computational scheme was applied for studying edge and screw dislocations in non-elemental systems for the first time. For the case of TiN as a model system, we established the preferred slip systems for edge and screw dislocations, with a Burgers vector of $a/2\langle 1\bar{1}0 \rangle$ on the $\{001\}$, $\{110\}$ and $\{111\}$ slip planes. The simulations adopted periodically repeating triclinic supercells containing a dipole of dislocations arranged such that periodicity can be maintained without imposition of large spurious elastic stresses. It was determined that the Peierls stress is the smallest for slip along the $\{110\}$ plane, and largest for slip along the $\{001\}$ plane, for both edge and screw dislocations. The dislocation core structures and the Peierls stress results are discussed and compared to those in a purely ionic MgO system.

© 2014 Acta Materialia Inc. Published by Elsevier Ltd. All rights reserved.

## 1. Introduction

Continuum elasticity has been very successful in describing the long-range fields of dislocations [1]. However, close to the dislocation core there are large lattice distortions and the linear elastic solution diverges [2]. The modeling of dislocation cores and their properties has been an active research field in materials physics. Atomistic simulations demonstrate that local forces at the dislocation core and their coupling to the applied stress can have a dramatic effect on structural properties [3]. This also applies to the Peierls stress, the minimum stress required to sustain the glide of dislocations through the crystal lattice [4]. Thus, accurate modeling of dislocation cores and the Peierls stress is key to the predictive modeling of the mechanical properties of materials.

In this paper, we employ electronic structure calculations based on density functional theory (DFT) to calculate the core structures and the Peierls stress for dislocations in titanium nitride (TiN). In recent years, multilayered nanocomposites made of TiN and Al have been used to explore the effect of layer thickness on hardness and flow strength [5–7]. It was found that, for a layer thickness of less than 5 nm, a high flow strength of 4.5 GPa and compressive deformability (5–7% plastic strain) are obtained in such layered composites. Understanding dislocation slip across the Al/TiN interface as well as through the TiN bulk is important to help interpret the experimental phenomena. In this paper, the DFT calculations aim to elucidate the preferred slip planes of dislocations in TiN, as well as providing measures of the resistance to the glide of dislocations in TiN.

For many ceramics, it is difficult to induce plastic flow [8]. TiN is an important engineering material, notably used as barrier layer material in the electronics industry. TiN is

---

* Corresponding author.
  *E-mail address:* xyliu@lanl.gov (X.-Y. Liu).

also a ceramic material that has complex bonding character, i.e. mixed covalent, ionic and metallic bonding. The mechanical properties of TiN thin films are of considerable interest and the measured hardness of TiN thin films at various film thicknesses is well determined [9]. However, surprisingly, there is little prior work on the preferred slip systems in TiN, either experimentally or theoretically. For bulk TiN, the material is brittle at temperatures below 750 °C [10], which might suggest that there is little or no dislocation activity in TiN below such temperature. However, experimentally, significant dislocation activities were observed at room temperature in Ti–TiN multilayer specimens for which the TiN layer is 150 nm in thickness [11]. Earlier, it was proposed that dislocations can nucleate and slip in ceramics at the nanoscale [12].

Modeling of dislocations in multi-element ceramic materials has been primarily done using shell model based empirical pair potentials. Modeling of core structures of dislocations in these materials has been used for strongly ionic materials where empirical pair potentials can reasonably describe the bonding, a typical example being MgO [13–15]. For TiN, where the bonding is complex enough that it cannot be considered as strongly ionic, reliable empirical pair potentials do not exist. Thus, DFT remains the only way to accurately describe dislocations in TiN.

Over the years, a number of DFT studies have been applied to predict the dislocation core structures and sometimes also applied to predict the Peierls stress of dislocations. Recent DFT efforts have concentrated on modeling of screw dislocations in pure body-centered cubic (bcc) metals, such as Fe, Mo and Ta [16–25], screw dislocations in bcc W alloys [26,27], dislocations (both edge and screw) in fcc Al [28] and dislocations in hexagonal close-packed (hcp) metals, including Mg (both edge and screw), Ti (screw) and Zr (screw) [29–33]. For non-metallic materials, DFT modeling of dislocations has been limited to single-element semiconductor materials, such as Si [34,35]. To the best of our knowledge, this is the first time that DFT has been used to study dislocation and its Peierls stress in a multi-element ceramic material.

Structurally, since TiN has a rock-salt (B1) crystal structure, the shortest possible Burgers vector is $a_0/2\langle 110 \rangle$, where $a_0$ is the lattice constant; however, the slip planes are not known. In this paper, we consider three low index planes, $(110)$, $(001)$ and $(111)$, as the possible slip planes. In ceramic materials with a rock-salt structure, we identified three materials that have experimentally determined preferred slip systems for comparison. One is in the case of a strongly ionic material, MgO, in which the preferred slip system is $1/2\langle 110 \rangle \{110\}$ followed by $1/2\langle 110 \rangle \{001\}$ [8]. Another one is in the case of AgCl, a strongly metallic material, in which a "pencil" slip of Burgers vector $a_0/2\langle 110 \rangle$ was observed [36]. Pencil slip is possible if slip can occur readily on $\{111\}$ planes or a combination of $\{100\}$, $\{110\}$ or $\{111\}$ planes. The third one is in the case of TiC$_x$. This material is closest to TiN in bonding chemistry. However, the strongly off-stoichiometric nature of

TiC$_x$ samples often seen in experiments makes the link to TiN somewhat unclear. Both $1/2\langle 110 \rangle \{110\}$ and $1/2\langle 110 \rangle \{111\}$ slip systems were observed to be active at low temperature in microhardness indentation experiments of TiC$_{0.91}$ by Chien et al. [37]. Previous DFT calculations show similar ideal shear strength in TiN in various shearing planes and directions [38].

To determine the Peierls stress, there are two approaches. One is based on the Peierls–Nabarro (PN) model [39–41], where the classical PN model [42,43] is used to calculate the dislocation core properties based on various assumptions [41]. This approach incorporates the generalized stacking fault (GSF) energy calculations into the solution of the PN equation, and has been applied to compute the Peierls stress of dislocations in MgO [44–46]. In this paper, we used the direct approach, i.e. we computed the Peierls stress from DFT simulations directly.

## 2. The details of the simulation procedure

Our DFT calculations were performed using the efficient planewave basis code Vienna ab initio Simulation Package (VASP) [47,48], employing the Perdew, Burke and Ernzerhof [49] exchange–correlation functional and the projector-augmented wave methodology [50]. To obtain accurate atomic forces and stresses, a $1 \times 1 \times 7$ Monkhorst–Pack mesh for k-point sampling and a planewave kinetic energy cutoff of 500 eV for the planewave expansion of the wave functions were used in all our supercell calculations. This relatively high number of k-points is identified to be required for our simulations, as DFT predicts TiN to be a metallic system. The calculated lattice parameter (0.424 nm) and bulk modulus (306 GPa) in the rock salt crystal structure [38] were in excellent agreement with other DFT calculations and experimental values [38,51]. The DFT computed elastic constants of TiN in the cubic axis are $C_{11} = 639$ GPa, $C_{12} = 139$ GPa and $C_{44} = 160$ GPa, in good comparison with experimental measured $C_{11} = 625$ GPa, $C_{12} = 165$ GPa and $C_{44} = 163$ GPa [52]. To compute the elastic constants in directions other than the cube axes, the elastic constant matrix is transformed according to $\{c'\} = \{\tilde{Q}\}\{c\}\{Q\}$, where $Q_{ijkl} = T_{ki}T_{lj}$ and $\{T\}$ is the transformation matrix between two sets of axes [2].

The initial atomic structure of dislocation was created using anisotropic elastic theory employing the Stroh solution [2]. The calculated elastic displacements are exact at large distances from the core (where the strain is infinitesimal), but are only approximate close to the core. For DFT calculations, a computational supercell employing the periodic boundary conditions is required. There have been several discussions in the literature on the periodic image effects in atomistic modeling of dislocations [17,24,53–56], mainly with examples on the screw dislocations. Introducing the dislocation dipole introduces a plastic strain of

$$\varepsilon_{ij} = \frac{(b_i A_j + b_j A_i)}{2S} \tag{1}$$

where $A$ is the dipole cut vector and $S$ is the area of the simulation supercell perpendicular to the dislocation line [18,53]. A homogeneous strain of opposite sign and equal to the plastic strain in magnitude is applied to the periodic supercell. In Fig. 1, a schematic diagram of dislocation(s) in a periodically repeating supercell is shown, with (a) quadrupole dislocations in supercell, and (b) a triclinic supercell with a dislocation dipole generating an array of dislocations identical to case (a). The advantage of a quadrupole array of dislocation arrangement is that the superposition of the elastic stress fields produces zero stress at any dislocation center. As shown in Fig. 1b, a quadrupole array of dislocation can be modeled using a dislocation dipole in the supercell by choosing a triclinic supercell [24]. For pure edge or screw dislocations, a simple procedure that is equivalent to Eq. (1) can be applied to the supercell to correct for the plastic strain. For the edge dislocation case in Fig. 1b, the length of the supercell along the Burgers vector $b$ direction can be chosen as $(2n + 1)|b|$, where $n$ is an integer. This is to make the triclinic supercell periodic, as the introduction of a single dislocation displaces the lattice in the upper half of the supercell by $b/2$ with respect to the lower half along the Burgers vector direction. Similarly, the introduction of screw dislocations also displaces the lattice in the upper half of the supercell by $b/2$ with respect to the lower half. So the supercell is tilted by $b/2$ to make the supercell periodic and still in a stress-free condition.

Owing to the above considerations, all the supercells in our DFT calculations adopt the triclinic supercell geometry, which contains a dislocation dipole in the supercell. The size of the supercell needs to be large enough to avoid core–core interaction. The dislocations are separated by a distance of ~2–3 nm away from each other in the supercells, with dimensions along $x$, $y$ and $z$ being 4–5, 3–4 and 0.3 nm, respectively, containing a total number of 312–468 atoms. This kind of computational setup makes the DFT calculations of the transition metal nitrides computationally intensive, especially with the relatively high number of k-points. Once the forces on each atom are converged using DFT, the correct geometry of the dislocation core is obtained. During all calculations, each component of the force on every atom was smaller than 0.05 eV Å$^{-1}$.

Once the equilibrium structure of dislocation cores in a supercell is determined, the Peierls stress is calculated by applying shear strain on the supercell. Shear strain is applied by distorting the supercell in the desired directions, in incremental steps, and the applied shear strain results in shear stress. The stress values are obtained from the DFT stress tensors in VASP calculations. These values eliminate the spurious Pulay stress by using a high energy cutoff (500 eV). Good agreement is obtained between the DFT stress and the estimate from the shear strain applied using the elastic anisotropic shear modulus of TiN in different crystal orientations. For edge dislocation calculations, the shear strain is applied in the plane containing the dislocation and along the Burgers vector of dislocations. For example, if the Peierls stress is to be estimated for the motion of dislocation in the $y$ plane and the Burgers vector is along the $x$ direction, then the shear strain applied is $\varepsilon_{yx}$. For screw dislocations, the shear strain is applied in the plane of motion of dislocations and along the Burgers vector. For example, if the Peierls stress is to be estimated for motion of a dislocation in the $y$ plane and the Burgers vector is along the $z$ direction, the shear strain applied is $\varepsilon_{yz}$. An alternative way to determine the Peierls stress is to use the nudged elastic band (NEB) method [57–59], e.g., using the recent proposed modification to the NEB method to calculate the Peierls stress [60]. However, we note that such a strategy is computationally expensive, and hence was not pursued here.

Once the Peierls stress is determined from DFT, a correction to the Peierls stress is applied. This correction is due to the attractive force between dipoles when perturbed from equilibrium quadrupolar configuration. A simple but qualitative estimation of the underestimation of Peierls stress can be given by an isotropic elasticity [2] correction to the calculated Peierls stress by considering only the stress fields from two neighboring dislocations. A more quantitative estimation of the underestimation of Peierls stress is given by anisotropic elasticity and to calculate the stress fields arising from an infinite array of dislocation dipoles due to periodic images. This is computed as the derivative of the elastic energy of the dislocation dipole with periodic arrangements with respect to the dislocation position. The methodology developed by Cai et al. [53,54] allows these anisotropic elastic calculations. Romaner et al. applied such methodology to compute the correction to Peierls stress in the DFT calculations of screw dislocations in W and showed that the corrected Peierls stress converges rapidly with supercell sizes [27]. In this work, we also carried out similar anisotropic elastic calculations to estimate the correction to the Peierls stress due to the small supercell sizes in DFT.
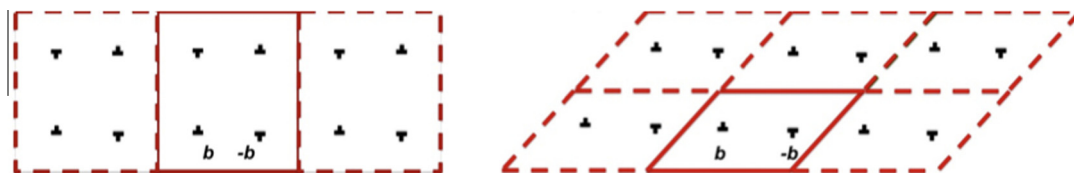


Fig. 1. Schematic diagram of dislocation dipoles in a periodically repeating supercell. Left: quadrupole dislocations in supercell; right: a triclininc supercell with a dislocation dipole.

## 3. Results and discussion

### 3.1. Core structure of edge dislocations

Fig. 2 shows the core structure of an $a_0/2[1\bar{1}0]$ (001) edge character dislocation in TiN, with (a) the atomic structure of the supercell, (b) the differential displacements (DDs) [61,62] and the Nye tensor distribution [63] for the dislocation and (c) a "bird's eye" examination of the dislocation core structure. The simulation supercell has the geometry of $x$ in $[1\bar{1}0]$, $y$ in $[001]$ and $z$ in $[110]$ directions. The dislocation line direction is in the $z$ direction. DDs show the relative displacement from a perfect lattice of two nearest neighbor atoms, projected along the Burgers vector direction by a vector of the corresponding length between the two atoms. The Nye tensor distribution computes the DDs between all nearest neighbor atoms, which produces a distribution of misfit or Burgers vector distribution. Such a distribution is projected onto the plane perpendicular to the dislocation line and is smoothly interpolated. The extrema in the Nye tensor distribution represent the dislocation core atoms. In this case, the core region includes two Ti and two N atoms at the extra half

plane side of the dislocation on the slip plane (Fig. 2b), indicating a compact core. The Nye tensor distribution plot also confirms our assumption of cores not interacting with each other during the DFT simulations. Fig. 2c shows a detailed examination of the dislocation core, with two lines that mark the continuous line of atoms in a nearly perfect crystal. Two extra half planes (one Ti and one N) are seen in between these lines. The criteria for the bonds between atoms to be shown for a pair of atoms are that the bond length be less than 2.6 Å. There are only two atoms in the core region that have a decrease of coordination number (from 6 to 5), presumably due to the highly rigid nature of the bonds. Due to the rigid bonding nature in ceramic, if the initial introduction of a dislocation into the crystal were not through anisotropic elasticity theory displacements, for example by a simply "half plane" cut, the resultant DFT relaxed dislocation core would be very different (not shown), with more atoms in the core region with low coordination numbers.

Fig. 3 shows the core structure of an $a_0/2[1\bar{1}0](110)$ edge character dislocation in TiN, also in (a) the atomic structure of the supercell, (b) the DD [61,62] and the Nye tensor distribution [63] for the dislocation and (c) a "bird's
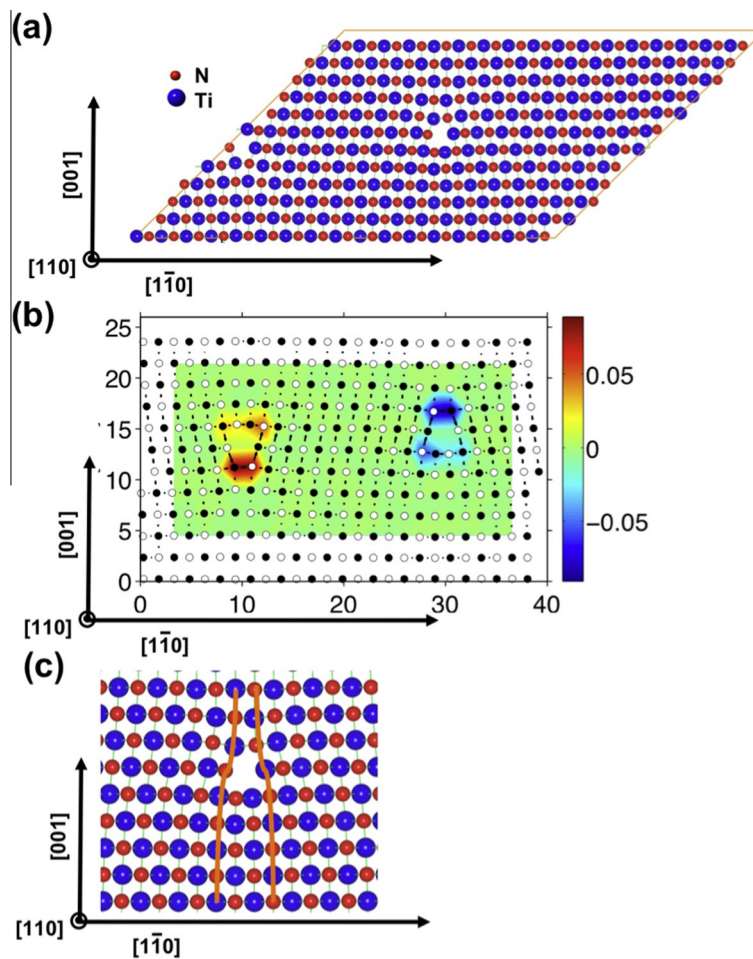


Fig. 2. (a) Atomic structure of the supercell containing a dipole of $a_0/2[1\bar{1}0](001)$ edge dislocations. Edge dislocations are marked in the supercell. (b) Nye tensor distribution of the corresponding supercell. (c) Atomic structure of a single edge dislocation.

eye" examination of the dislocation core structure. The simulation supercell has the geometry of $x$ in $[1\bar{1}0]$, $y$ in $[110]$ and $z$ in $[001]$ directions. The dislocation line direction is again in the $z$ direction. It is noted that the core of this dislocation is more extended than the $a_0/2[1\bar{1}0](001)$ edge dislocation. Fig. 3c shows a detailed examination of the dislocation core, with two lines that mark the continuous line of atoms in a nearly perfect crystal. The core region contains up to five Ti and five N atoms at the extra half plane side of the dislocation on the slip plane, indicating an extended core. Again, the bonds are shown for pairs of atoms with a distance of less than 2.6 Å, and two N and two Ti atoms have a decrease of coordination number from 6 to 5. This core structure is essentially the same as the core structure found in previous atomistic studies of MgO using empirical potential [15].

Fig. 4 shows the core structure of an $a_0/2[1\bar{1}0](111)$ edge character dislocation in TiN, again in (a) the atomic structure of the supercell, (b) the DD [61,62] and the Nye tensor distribution [63] for the dislocation and (c) a "bird's eye" examination of the dislocation core structure. The simulation supercell has the geometry of $x$ in $[1\bar{1}0]$, $y$ in $[111]$ and $z$ in $[11\bar{2}]$ directions, with the dislocation line direction again in the $z$ direction. A detailed disregistry analysis along the slip plane is also shown in Fig. 4d. Both the disregistry analysis and the Nye tensor plot suggested that this edge dislocation dissociates into two partial dislocations. We have also carried out DFT calculations of the

generalized stacking fault energy calculations [64] on (111) planes, which is to be published elsewhere. On (111) planes, the DFT results of the generalized stacking fault energy as a function of displacements along the $\langle 11\bar{2}\rangle$ plane demonstrate a stable stacking fault at an $a_0/3\langle 112\rangle$ displacement [64]. The dislocation dissociation is

$$\frac{a_0}{2}\langle 1\bar{1}0\rangle = \frac{a_0}{6}\langle 2\bar{1}1\rangle + \frac{a_0}{6}\langle 1\bar{2}\bar{1}\rangle \qquad (2)$$

Using isotropic linear elasticity analysis, based on the stacking fault energy of 1.09 J m$^{-2}$, the estimated separation distance between the two partials is 0.8 nm, or less than three times that of the Burgers vector length in the $\langle 110\rangle$ direction. For such a short separation distance, it is conceivable that the atomistic calculated separation distance between the partial dislocations may be smaller than this value, due to a strong influence from the dislocation cores. Taking this factor into consideration, the agreement between the estimated partial separation distance value and that from the DFT calculated cores (0.4–0.7 nm) is reasonably good.

Fig. 4c shows a detailed examination of the dislocation core, with two lines that mark the continuous line of atoms in a nearly perfect crystal. The two dislocations in the supercell are not equal to each other since one is "N terminated", and the other is "Ti terminated" at the slip plane. This is due to the dipole arrangement of the supercell. Both dislocations show clear splitting of partials. Interestingly,
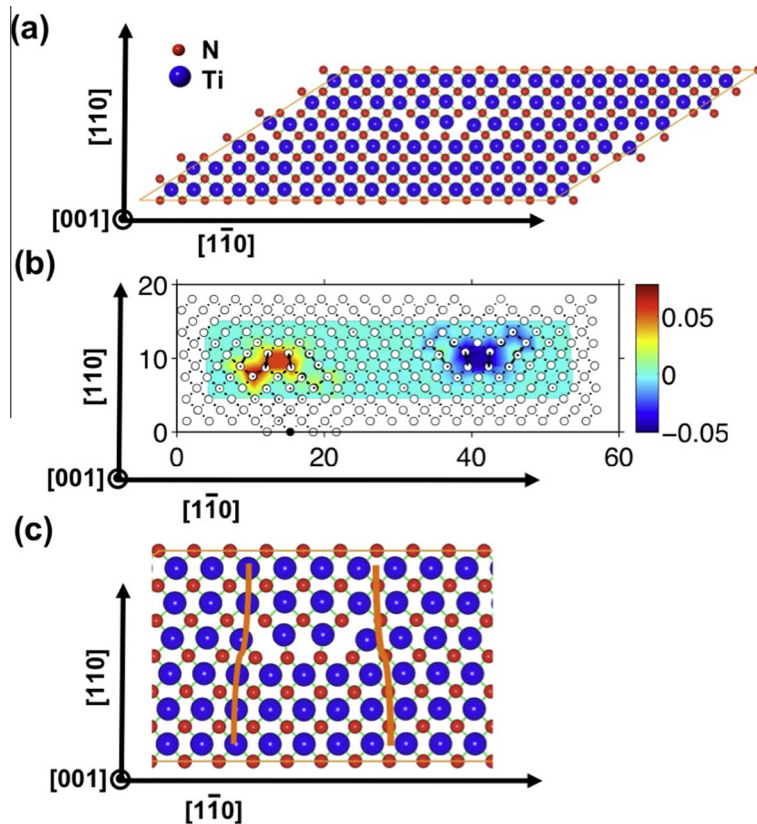


Fig. 3. (a) Atomic structure of the supercell containing a dipole of $a_0/2[1\bar{1}0](110)$ edge dislocations. (b) Nye tensor distribution of the corresponding supercell. (c) Atomic structure of a single edge dislocation.
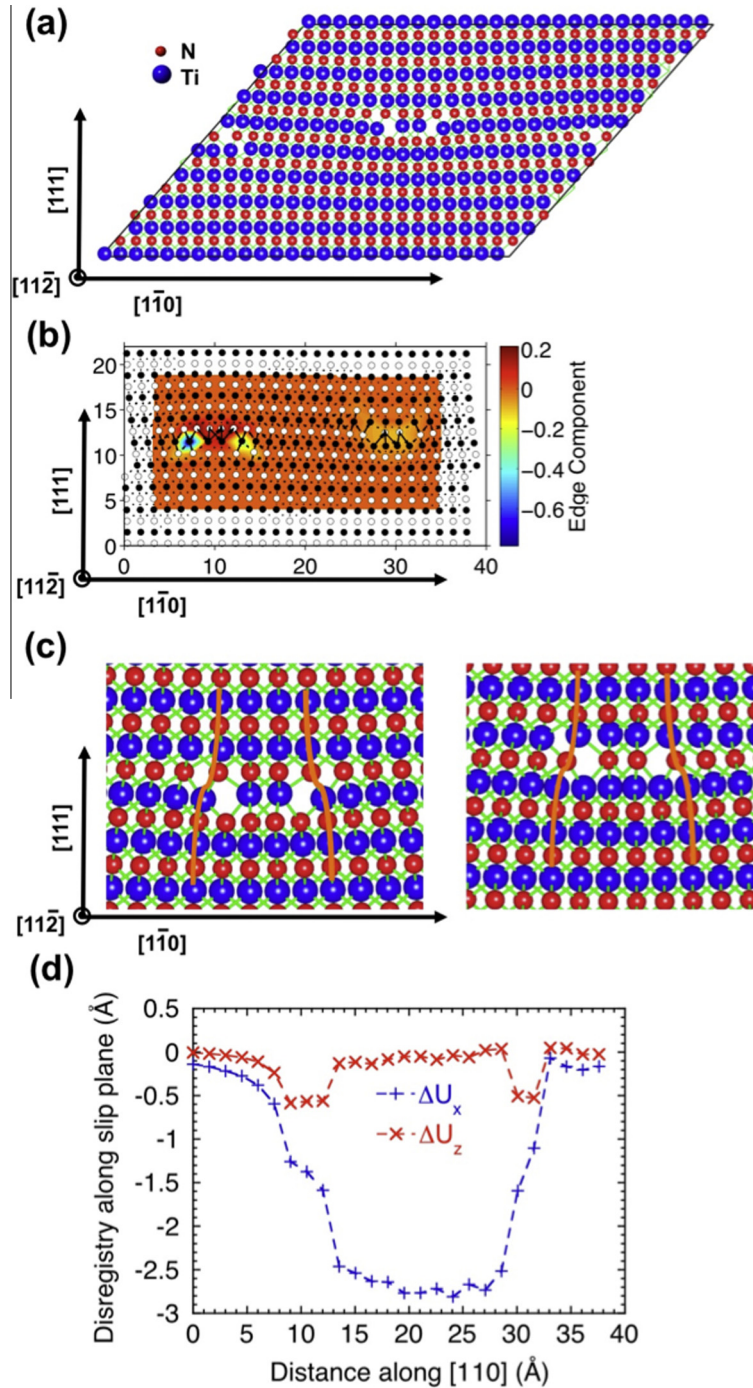
Fig. 4. (a) Atomic structure of the supercell containing a dipole of $a_0/2[1\bar{1}0](1\,1\,1)$ edge dislocations. (b) Nye tensor distribution of the corresponding supercell. Atomic structure of a single edge dislocation with (c) (left) N termination and (right) Ti termination. (d) Disregistry along the slip plane of N-termination dislocation in (c).

inside both dislocation cores, no atom has a coordination number different from that of bulk, due to the splitting of a dislocation into two partials.

### 3.2. Peierls stress of edge dislocations

To calculate the Peierls stress on a given plane of edge dislocations with Burgers vector $a_0/2[1\bar{1}0]$, shear strain is applied on $(0\,0\,1)$, $(1\,1\,0)$ and $(1\,1\,1)$ planes along $[1\bar{1}0]$.

After the introduction of dislocations, both the lattice vectors and the internal atomic positions of the computational supercell are relaxed, so it is stress free. Then shear strain is applied by tilting the lattice vectors of the supercell in the desired directions. The initial value of the resultant shear stress can be estimated using elastic constants and the applied shear strain, which is found to be comparable to the DFT stress in the supercell. Since a limited number of DFT calculations was performed, these values are

reported as a range. The lower number represents the largest value of the shear stress for which the dislocation did not move, while the higher number represents the stress at which the dislocation moved by at least half a Burgers vector. For an $a_0/2\langle 110 \rangle\{110\}$ edge dislocation, it was determined that the Peierls stress $\tau_p^{\text{DFT}}$ is between 0.5 and 0.6 GPa. For the $a_0/2\langle 110 \rangle\{111\}$ edge dislocation, it was determined that the Peierls stress $\tau_p^{\text{DFT}}$ is between 1.7 and 2.2 GPa. For the $a_0/2\langle 110 \rangle\{001\}$ edge dislocation, the DFT calculated Peierls stress $\tau_p^{\text{DFT}}$ is between 7.9 and 8.8 GPa.

Table 1 lists both the uncorrected DFT Peierls stress ($\tau_p^{\text{DFT}}$), the correction to the calculated value ($\Delta\tau_p^{\text{DFT}}$) and the corrected Peierls stress ($\tau_p^{\text{DFT}} + \Delta\tau_p^{\text{DFT}}$). After correction, the lowest Peierls stress obtained for edge dislocations is 1.3–1.4 GPa for the $a_0/2[1\bar{1}0](110)$ slip system. The second lowest Peierls stress obtained is 2.7–3.2 GPa for the $a_0/2[1\bar{1}0](111)$ slip system, and the highest Peierls stress (8.7–9.6 GPa) is for the $a_0/2[1\bar{1}0](001)$ slip system. For the $a_0/2[1\bar{1}0](111)$ edge character dislocation in TiN, the dislocation with "Ti terminated" at the slip plane glides more than the "N terminated" dislocation. The correction to stress computed is thus an upper limit.

For comparison, the Peierls stresses for edge dislocations in MgO as determined from the classical P–N model using DFT inputs of GSF energies are 0.08 GPa for the $a_0/2[1\bar{1}0](110)$ slip system and 0.3 GPa for the $a_0/2[1\bar{1}0]$ $(001)$ slip system [45]. The Peierls stress for the $a_0/2[1\bar{1}0]$ $(111)$ edge dislocation is not determined but is assumed to be of a higher value since experimentally the slip for this dislocation is not observed. First, it is noticed that the lowest Peierls stress slip system for both TiN and MgO is $1/2[1\bar{1}0](110)$; however, the second lowest Peierls stress slip system is different. Second, both values are smaller than those for the corresponding TiN slip systems. Third, we'd also like to comment on the relationship of the Peierls barriers and the hardness measurements in these materials. For the case of MgO, the nominally pure single crystal with (100) orientation has a hardness of 9.2 GPa [65]. For TiN, the reported typical hardness ranging from 17.3 to 22.1 GPa for (001) and (011), and from 19.8 to 23.8 GPa for (111) orientation [9]. The normal stress is 1/3 of the hardness. To get shear stress on a specific slip system, a Schmid factor is multiplied to the normal stress. The Schmid factors for both MgO and TiN are 0.25, 0.5 for loading along [011] and [001] for the most possible slip system, $\frac{1}{2}[1\bar{1}0](110)$ [9]. So the hardness data along (100) or (011) orientations should be divided by a factor

of 6 or 12, in order to make a comparison to the Peierls stress values. For the MgO case, the shear stress from the reported hardness is much larger than the Peierls stress values for possible active slip systems. One possible reason is due to the lack of a high density of dislocations in these ceramic materials so the hardness is more related to the nucleation barrier of dislocations rather than the Peierls barriers. For TiN cases, the shear stress from the reported hardness is larger than the Peierls stress values for the most preferred slip system $1/2[1\bar{1}0](110)$, but close to the Peierls stress values for the second preferred slip systems, $1/2[1\bar{1}0](111)$. Hardness also includes strain hardening, which is not accounted here.

### 3.3. Core structure of screw dislocation

Similar to edge dislocations, we consider screw dislocations with Burgers vector $a_0/2[110]$. The simulation supercell has the geometry of $x$ in $[\bar{1}\bar{1}2]$, $y$ in $[111]$ and $z$ in $[1\bar{1}0]$ directions. The dislocation line direction is in the $z$ direction. The screw dislocation in TiN is found to spread in the $\{110\}$ plane, leading to the dislocation core structure in Fig. 5, which shows a differential displacement map [61,62] of the core structure of the $a_0/2[1\bar{1}0]$ screw character dislocation in TiN. On the differential displacement map, only the displacement along the Burgers vector is plotted. The strong asymmetry in the screw dislocation core spread is also observed in the P–N model analysis of the screw dislocation in MgO based on the generalized stacking fault energies from DFT as inputs [46]. The different bonding nature in TiN compared to MgO does not change such features of the core structure of the $a_0/2[1\bar{1}0]$ screw dislocation.

### 3.4. Peierls stress of screw dislocation

To calculate the Peierls stress of the screw dislocation with Burgers vector $a_0/2[1\bar{1}0]$ along different slip planes, shear strain is applied on $(001)$, $(110)$ and $(111)$ planes along $[1\bar{1}0]$. After the introduction of the dislocation, again, both the lattice vectors and the internal atomic positions of the computational supercell are relaxed so it is stress free before the shear strain is applied.

We first applied shear strain on a simulation supercell for the dislocation to glide on $(110)$. The simulation is set up with a triclinic supercell containing a dislocation dipole as described earlier, with $x$ in $[001]$, $y$ in $[110]$ and $z$ in $[1\bar{1}0]$ directions. The dislocation line is in the $z$

Table 1
The Peierls stress of edge dislocations calculated for various slip systems in TiN, the P–N equation model estimated Peierls stress in MgO and, for $\Delta\tau_p^{\text{DFT}}$ calculations, the results of anisotropic elasticity with periodic images.

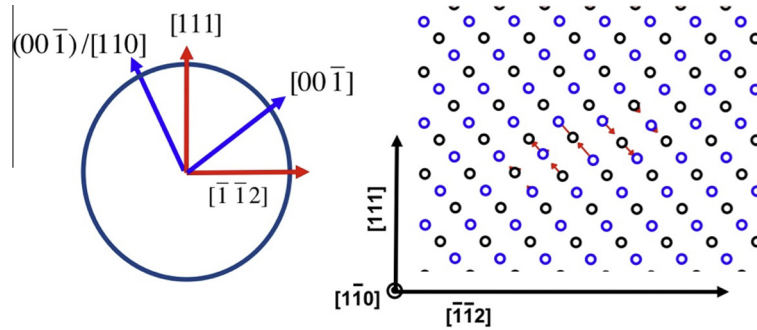| Slip system | $\tau_p^{\text{DFT}}$ (GPa) | $\Delta\tau_p^{\text{DFT}}$ (GPa) | $\tau_p^{\text{Total}}$ (GPa) | $\tau_p$ (GPa) (MgO) |
|---|---|---|---|---|
| $\langle 110 \rangle\{110\}$ | 0.5–0.6 | 0.83 | 1.3–1.4 | 0.08 [45] |
| $\langle 110 \rangle\{111\}$ | 1.7–2.2 | 0.96 | 2.7–3.2 | |
| $\langle 110 \rangle\{001\}$ | 7.9–8.8 | 0.82 | 8.7–9.6 | 0.3 [45] |

Fig. 5. Differential displacement map of the screw dislocations. Black and blue dots represent Ti and N atoms, respectively. (For interpretation of the references to colour in this figure legend, the reader is referred to the web version of this article.)

direction. Since the $a_0/2[1\bar{1}0]$ screw dislocation has a core spread mainly in the (110) plane, we expect the Peierls barrier of the dislocation glide on this plane to be the lowest. The applied shear strain $\varepsilon_{yz}$ induces Peach–Koehler forces in the $x$ direction and screw dislocation moves in the (110) plane. It was determined that the critical shear stress is between 0.3 and 0.6 GPa. We use the differential displacement map to show movement of the screw dislocation. In Fig. 6a, it is clearly shown that after the critical shear stress, a movement of screw dislocation on the (110) plane is observed.

Next we also set up a simulation supercell to allow the $a_0/2[1\bar{1}0]$ screw dislocation to glide on the (111) plane, with $x$ in $[\bar{1}\bar{1}2]$, $y$ in [111] and $z$ in $[1\bar{1}0]$ directions. The applied shear strain $\varepsilon_{yz}$ should induce Peach–Koehler forces in the $x$ direction and the dislocation is expected to move in the (111) plane. However, since this force has a component on the neighboring (110) plane by an angle of 35.26° and the Peierls stress of the screw dislocation to glide along the (110) plane is small enough, it was observed that the dislocation moved on the (110) plane instead. Fig. 6b shows the movement of the screw dislocation on the (110) plane.

Finally, we set up a simulation supercell to allow the $a_0/2[1\bar{1}0]$ screw dislocation to glide on the (001) plane, with $x$ in [110], $y$ in [001] and $z$ in $[1\bar{1}0]$ directions. The shear strain $\varepsilon_{yz}$ is applied on the supercell so the dislocation is expected to move on the (001) plane. In this case, the dislocation was found to move on the neighboring (111) plane, which has an angle of 54.74° with the (001) plane. Fig. 7 shows movement of such a screw dislocation on the (111) plane after the critical shear stress was applied. The critical shear stress is between 10.3 and 14.9 GPa. This leads to the DFT calculated Peierls stress $\tau_p^{DFT}$ of the screw dislocation along the (111) slip plane between 8.6 and 9.2 GPa. And it is estimated that the Peierls stress $\tau_p^{DFT}$ of the screw dislocation along the (001) slip plane is greater than 14.9 GPa.

In Table 2, both the uncorrected DFT Peierls stress ($\tau_p^{DFT}$) and the correction to the calculated value ($\Delta\tau_p^{DFT}$) and the corrected Peierls stress ($\tau_p^{DFT} + \Delta\tau_p^{DFT}$) for the slip systems are listed. The lowest Peierls stress obtained for screw dislocations is 0.4–0.7 GPa for the $a_0/2[1\bar{1}0](110)$ slip system. The second lowest Peierls stress obtained is 9.0–9.5 GPa for the $a_0/2[1\bar{1}0](111)$ slip system. And the highest Peierls stress is for the $a_0/2[1\bar{1}0](001)$ slip system, more than 15.3 GPa. For comparison, the Peierls stresses for screw dislocations in MgO as determined from the classical P–N model using DFT inputs of GSF energies are 0.15 GPa for the $a_0/2[1\bar{1}0](110)$ slip system and 1.6 GPa for the $a_0/2[1\bar{1}0](001)$ slip system [45]. The trend in the screw dislocation is similar to the edge dislocation case discussed earlier. In TiN, the lowest Peierls barrier of the screw dislocation is comparable to that of the edge dislocation. However, it is noted that for the screw dislocation, the second lowest Peierls barrier (slip along (111)) is much higher than the edge dislocation counterpart by a large quantity, ∼6.3 GPa.

## 4. Summary

Using the state-of-the-art DFT-based first-principles method, the core structure and Peierls stress of both edge and screw character dislocations in bulk TiN were modeled. To the best of our knowledge, this is the first time that DFT has been used to study dislocation and its Peierls stress in a multi-element ceramic material. We used the direct approach to compute the Peierls stress from DFT simulations, adopting the triclinic supercell geometry, which contains a dislocation dipole in the supercell. We estimated the correction to the Peierls stress computed from DFT which is due to the attractive force between dipoles when perturbed from an equilibrium quadrupolar configuration.

For the case of TiN as a model system, we established the preferred slip systems for edge and screw dislocations, with a Burgers vector of $a/2\langle1\bar{1}0\rangle$ on the {001}, {110} and {111} slip planes. It was determined that the Peierls stress is the smallest for slip along the {110} plane, and largest for slip along the {001} plane, for both edge and screw dislocations. In comparison to the preferred slip systems in MgO, the lowest Peierls stress slip system for both TiN and MgO is $1/2[1\bar{1}0](110)$. However, the second lowest Peierls stress slip system in TiN is $1/2[1\bar{1}0](111)$ and $1/2[1\bar{1}0](001)$ in MgO. This is presumably due to the bonding of TiN, which caused the $a_0/2[1\bar{1}0](111)$ edge
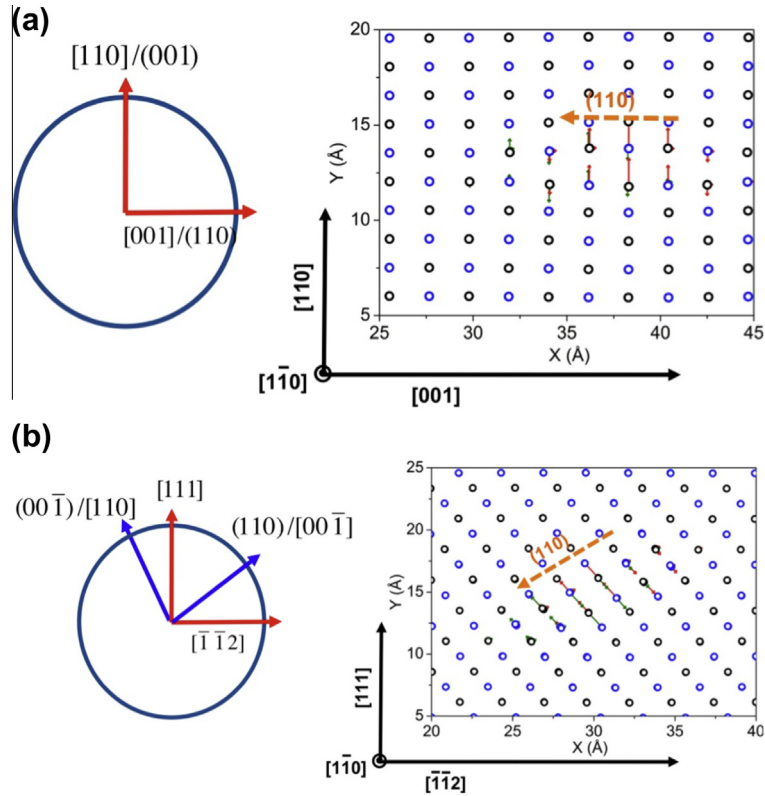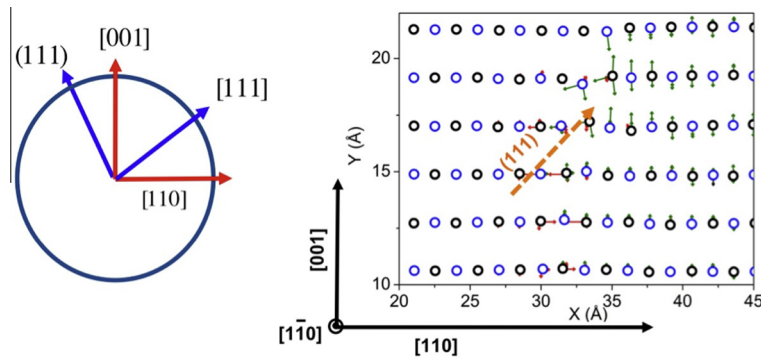
Fig. 6. (a) Movement of screw dislocation in the (1 1 0) plane. (b) Movement of dislocation in the (1 1 0) plane. Though shear is applied to move in the (1 1 1) plane the dislocation moves in the (1 1 0) plane, as the Peierls stress is small. Red and green arrows represent equilibrium and displaced screw dislocation, respectively. (For interpretation of the references to colour in this figure legend, the reader is referred to the web version of this article.)



Fig. 7. Movement of dislocation in the (1 1 1) plane (though shear is applied so that the screw dislocation moves in the (0 0 1) plane). Red and green arrows represent equilibrium and displaced screw dislocation, respectively. (For interpretation of the references to colour in this figure legend, the reader is referred to the web version of this article.)

Table 2
Peierls stress of screw dislocations calculated for various slip systems in TiN, the P–N equation model estimated Peierls stress in MgO and, for $\Delta\tau_p^{DFT}$ calculations, the results for anisotropic elasticity with periodic images.

| Slip system | $\tau_p^{DFT}$ (GPa) | $\Delta\tau_p^{DFT}$ (GPa) | $\tau_p^{Total}$ (GPa) | $\tau_p$ (GPa) (MgO) |
|---|---|---|---|---|
| $\langle 1\,1\,0\rangle\{1\,1\,0\}$ | 0.3–0.6 | 0.13 | 0.4–0.7 | 0.15 [45] |
| $\langle 1\,1\,0\rangle\{1\,1\,1\}$ | 8.6–9.2 | 0.37 | 9.0–9.5 | |
| $\langle 1\,1\,0\rangle\{0\,0\,1\}$ | >14.9 | 0.37 | >15.3 | 1.6 [45] |

dislocation to dissociate into two partial dislocations. It is also noted that the Peierls barriers in TiN are higher than the corresponding slip systems in MgO. In TiN, the lowest

Peierls barrier of the screw dislocation is comparable to that of the edge dislocation. However, it is noted that for the screw dislocation, the second lowest Peierls barrier with

slip along (1 1 1) is much higher than the edge dislocation counterpart.

The study presented here is envisioned to shed light on the preferred slip systems in TiN. In the future, a comparative study using other DFT based approaches such as the Greens functions approach [23,29] will also be useful.

## Acknowledgements

## References

[1] Hull D, Bacon DJ. Introduction to dislocations. Oxford: Butterworth-Heinemann; 2001.
[2] Hirth JP, Lothe J. Theory of dislocations. New York: McGraw-Hill; 1982.
[3] Woodward C. Mater Sci Eng A Struct 2005;400:59.
[4] Hoagland RG, Hirth JP, Gehlen PC. Philos Mag 1976;34:413.
[5] Bhattacharyya D, Mara NA, Dickerson P, Hoagland RG, Misra A. Acta Mater 2011;59:3804.
[6] Bhattacharyya D, Mara NA, Dickerson P, Hoagland RG, Misra A. Philos Mag 2010;90:1711.
[7] Bhattacharyya D, Mara NA, Hoagland RG, Misra A. Scr Mater 2008;58:981.
[8] Mitchell TE, Heuer AH. In: Nabarro FRN, Hirth JP, editors. Dislocations in solids. Amsterdam: Elsevier; 2005. p. 339.
[9] Ljungcrantz H, Oden M, Hultman L, Greene JE, Sundgren JE. J Appl Phys 1996;80:6725.
[10] Yamada T, Simada K, Koizumi M. Am Ceram Soc Bull 1980;59:611.
[11] Kumar S, Wolfe DE, Haque MA. Int J Plast 2011;27:739.
[12] Gerberich WW, Michler J, Mook WM, Ghisleni R, Ostlund F, Stauffer DD, et al. J Mater Res 2009;24:898.
[13] Walker AM, Gale JD, Slater B, Wright K. Phys Chem Chem Phys 2005;7:3227.
[14] Walker AM, Gale JD, Slater B, Wright K. Phys Chem Chem Phys 2005;7:3235.
[15] Zhang FW, Walker AM, Wright K, Gale JD. J Mater Chem 2010;20:10445.
[16] Ismail-Beigi S, Arias TA. Phys Rev Lett 2000;84:1499.
[17] Clouet E, Ventelon L, Willaime F. Phys Rev Lett 2009;102:055502.
[18] Clouet E, Ventelon L, Willaime F. Phys Rev B 2011;84:224107.
[19] Clouet E, Ventelon L, Willaime F. Phys Rev B 2012;85:029902.
[20] Ventelon L, Willaime F. Philos Mag 2010;90:1063.
[21] Ventelon L, Willaime F. J Comput Aided Mater 2007;14:85.
[22] Frederiksen SL, Jacobsen KW. Philos Mag 2003;83:365.
[23] Woodward C, Rao SI. Philos Mag A 2001;81:1305.
[24] Li J, Wang C-Z, Chang J-P, Cai W, Bulatov VV, Ho K-M, et al. Phys Rev B 2004;70:104113.
[25] Weinberger CR, Tucker GJ, Foiles SM. Phys Rev B 2013;87: 054114.
[26] Li H, Wurster S, Motz C, Romaner L, Ambrosch-Draxl C, Pippan R. Acta Mater 2012;60:748.
[27] Romaner L, Ambrosch-Draxl C, Pippan R. Phys Rev Lett 2010: 104.
[28] Woodward C, Trinkle DR, Hector LG, Olmsted DL. Phys Rev Lett 2008;100:045507.
[29] Yasi JA, Nogaret T, Trinkle DR, Qi Y, Hector LG, Curtin WA. Model Simul Mater Sci 2009;17:055012.
[30] Ghazisaeidi M, Trinkle DR. Acta Mater 2012;60:1287.
[31] Tarrat N, Benoit M, Morillo J. Int J Mater Res 2009;100:329.
[32] Clouet E. Phys Rev B 2012;86:144104.
[33] Shin I, Carter EA. Model Simul Mater Sci 2012:20.
[34] Pizzagalli L, Beauchamp P. Philos Mag Lett 2004;84:729.
[35] Pizzagalli L, Beauchamp P, Jonsson H. Philos Mag 2008;88:91.
[36] Vavra F. Czech J Phys B 1972;22:138.
[37] Chien FR, Ning XJ, Heuer AH. Acta Mater 1996;44:2265.
[38] Yadav SK, Ramprasad R, Misra A, Liu XY. J Appl Phys 2012;111:083505.
[39] Bulatov VV, Kaxiras E. Phys Rev Lett 1997;78:4221.
[40] Lu G, Kioussis N, Bulatov VV, Kaxiras E. Philos Mag Lett 2000;80:675.
[41] Schoeck G. Mater Sci Eng A Struct 2005;400:7.
[42] Peierls RE. Proc Phys Soc Lond 1940;52:34.
[43] Nabarro FRN. Proc Phys Soc Lond 1947;59:256.
[44] Carrez P, Ferre D, Cordier P. Model Simul Mater Sci 2009:17.
[45] Amodeo J, Carrez P, Cordier P. Philos Mag 2012;92:1523.
[46] Amodeo J, Carrez P, Devincre B, Cordier P. Acta Mater 2011;59:2291.
[47] Kresse G, Furthmuller J. Comput Mater Sci 1996;6:15.
[48] Kresse G, Hafner J. Phys Rev B 1993;47:558.
[49] Perdew JP, Burke K, Ernzerhof M. Phys Rev Lett 1996;77:3865.
[50] Blochl PE. Phys Rev B 1994;50:17953.
[51] Bhattacharyya D, Liu XY, Genc A, Fraser HL, Hoagland RG, Misra A. Appl Phys Lett 2010:96.
[52] Kim JO, Achenbach JD, Mirkarimi PB, Shinn M, Barnett SA. J Appl Phys 1992;72:1805.
[53] Cai W, Bulatov VV, Chang JP, Li J, Yip S. Philos Mag 2003;83: 539.
[54] Cai W, Bulatov VV, Chang JP, Li J, Yip S. Phys Rev Lett 2001;86:5727.
[55] Lehto N, Oberg S. Phys Rev Lett 1998;80:5568.
[56] Liu XY, Wang J, Biner SB. Model Simul Mater Sci 2008:16.
[57] Henkelman G, Jonsson H. J Chem Phys 2000;113:9978.
[58] Henkelman G, Uberuaga BP, Jonsson H. J Chem Phys 2000;113: 9901.
[59] Jonsson H, Mills G, Jacobsen KW. In: Berne BJ, Ciccotti G, Coker DF, editors. Classical and quantum dynamics in condensed phase simulations. Singapore: World Scientific; 1998. p. 385.
[60] Groger R, Vitek V. Model Simul Mater Sci 2012:20.
[61] Vitek V, Perrin RC, Brown DK. Philos Mag 1970;21:1049.
[62] Vitek V. Cryst Lattice Defects 1974;5:1.
[63] Hartley CS, Mishin Y. Acta Mater 2005;53:1313.
[64] Yadav SK, Liu XY, Wang J, Ramprasad R, Misra A, Hoagland RG. Philos Mag 2014;94:464.
[65] Caceres D, Vergara I, Gonzalez R. Philos Mag A 2002;82:1159.